# Sheet-on-sheet like calcium ferrite and graphene nanoplatelets nanocomposite: A multifunctional nanocomposite for high-performance supercapacitor and visible light driven photocatalysis

**M. Israr[a, b], Javed Iqbal[a,*], Aqsa Arshad[c], P. Gómez-Romero[b]**

[a]LNT, Department of Physics, Quaid-i-Azam University, Islamabad, Pakistan
[b]Catalan Institute of Nanoscience and Nanotechnology, Autonomous University of Barcelona, Spain
[c]Department of Physics, International Islamic University, Islamabad, Pakistan

*Corresponding author: javed.saggu@qau.edu.pk

## Abstract

The calcium ferrite-graphene nanoplatelets nanocomposites with sheet-on-sheet like morphology are fabricated and investigated for their physiochemical characteristics, electrochemical energy storage capacity and photocatalysis. Interestingly, the $(CF)_{1-x}(GNPs)_x$ nanocomposite-based electrode has shown maximum specific capacitance up to 422 $Fg^{-1}$ at 0.25 $Ag^{-1}$ with excellent cycling stability, 2.6 times higher than that of neat CF nanosheets. Furthermore, the synergistic contribution from photocatalytic and photo-Fenton reactions enables $(CF)_{1-x}(GNPs)_x$ nanocomposites to offer superior photocatalytic activity (99.4% dye removal in 90 min). The inclusion of GNPs significantly enhances the charge carriers separation and transportation. The excellent electrochemical efficiency of $(CF)_{1-x}(GNPs)_x$ could be attributed to the 2D interfacial interactions that provide a better charge transport at electrode/electrolyte interface . These interactions are also responsible for creating effective charge transport pathways and efficient $e^-/h^+$ separation leading to rapid dye-degradation, which make the material potential for remediation of water pollution and energy storage systems.

**Keywords:** Graphene ferrites nanocomposite; Nanosheets; Energy storage; Photocatalysis

## 1. Introduction

The ever-increasing demand for eco-friendly, efficient, and cost-effective renewable energy has motivated the development of innovative systems for energy storage [1, 2]. In particular, the electrochemical supercapacitors are emerging as effective energy storage devices in many electronics markets, due to their potential merits of rapid charge-discharge capability, high power output, and outstanding cycling stability [3]. To combat environmental safety risks and high production cost of traditional energy storage materials, the researchers have focused their attention on the development of novel energy materials, that could take up these issues [4, 5]. Multi-cation transition metal oxides, like metal ferrites, have certain promising features to be used in electrochemical energy storage applications because of their large theoretical capacity and diversity in structural morphology [6-9]. However, their use is limited due to their high

resistivity and electrode pulverization, which results in electrical insulation and poor cycling stability [10]. To overcome these drawbacks, graphene with its unique properties can be used as a conductive backbone for the modification of ferrite nanostructures [11]. Combination of 2D carbon materials like g-$CN_3$, graphene. 0D, 1D, and other 2D nanostructures in the form of nanocomposites are expected to optimize their physicochemical properties effectively [12-18]. Particularly, the composites of graphene with 2D nanostructures is expected to significantly tune the efficiency of nanocomposites in the applications, where a high level of surface interactions are crucial e.g., in supercapacitors, solar energy conversion and photocatalysis process [19].

Photocatalysis offers one of the most viable solutions for environmental remediation through abundant solar power having extra advantages of fast pollutant degradation and eco-friendliness [20]. Notably, the visible-light-drive photocatalysis is particularly effective for harvesting abundantly available solar light as compared to the processes based on UV visible light [21]. In this regard, the spinel ferrites, in combination with graphene, could be a fascinating choice as visible light active photo-stable photocatalysts [22]. Here, it is important to mention that the fast charge recombination, aggregation, and poor conductivity of neat ferrite nanostructures stimulate the need for compositing graphene with these materials [23]. This could help to establish the synergistic effects of both components in one material [24].

Among metal ferrites, spinel $CaFe_2O_4$ (CF) is a non-toxic and biocompatible p-type semiconductor, having visible light response with a relatively low energy band gap (1.9 eV) and suitable conduction band minimum (−0.6 V vs RHE) [25-27]. These properties make CF promising for applications in electrochemical sensors [28, 29], Li-ion batteries [30], water splitting [31, 32], photocatalysis [33], dye adsorption [34] and catalysis [35]. However, CF has relatively low quantum efficiency due to the aggregation and low conductivity issues. Therefore, it would be advantageous to fabricate graphene based CF nanocomposites, instead of using bare CF nanostructures [36]. The use of graphene as a 2D support will be promising because of its highly conducting nature, which is significantly helpful for achieving materials with improved performance as an electrochemical electrode material and photocatalyst [37]. To further enhance the performance of the composite material strong electronic and chemical interactions via formation of the 2D interfacial contact between CF and graphene is highly desired in these applications [38-42].

Herein, a facile, cost-effective in-situ co-precipitation method has been utilized to anchor CF nanosheets onto GNPs for supercapacitor and photocatalytic applications [43]. The electrochemical measurements suggest that the prepared nanocomposites exhibit better supercapacitive performance due to fast interfacial charge transfer at the 2D nano-interfaces. Importantly, the prepared nanocomposites have demonstrated improved charge separation and transportation characteristics, which lead to the significant augmentation in visible-light driven photocatalytic activity. The origin of the outstanding performance enhancement is thoroughly investigated and explained on the basis of physiochemical characteristics of the $(CF)_{1-x}(GNPs)_x$ nanocomposite, improved interfacial charge transfer, reduced agglomeration, and suppressed

recombination of charge carriers. To our knowledge this work, for the first-time reports, a combined study on multifunctional CF/GNPs nanocomposites with sheet on sheet like morphology, that investigates the supercapacitor and photocatalytic applications of $(CF)_{1-x}(GNPs)_x$ composites.

## 2. Experimental Methods

### 2. 1. Materials

Analytical grade iron chloride hexahydrate ($FeCl_3 \cdot 6H_2O$), calcium chloride hexahydrate ($CaCl_2 \bullet 6H_2O$), sodium hydroxide (NaOH), cetrimonium bromide (CTAB) and graphene nanoplatelets (GNPs), all Sigma-Aldrich products, were utilized without further purifications. Distilled water (DW) was used for the synthesis procedures. All the synthesis has been carried out using distilled water as a solvent.

### 2. 2. Preparation of $(CF)_{1-x}(GNPs)_x$ nanocomposites

The $(CF)_{1-x}(GNPs)_x$ nanocomposites having different loading of GNPs (0, 25, 50, 75, 100 wt. %) have been synthesized using CTAB assisted in-situ coprecipitation method. In a typical procedure $(CF)_{0.75}(GNPs)_{0.25}$ nanocomposite has been synthesized as follows: 300 mg GNPs were homogeneously mixed with aqueous solution of CTAB (0.1 g) and NaOH (6 M) using ultrasonic treatment. Then the formed mixture was heated to 80°C. To the above mixture the solution containing $FeCl_3 \bullet 6H_2O$ (100 mM) and $CaCl_2 \bullet 6H_2O$ (50 mM) was added drop by drop under magnetic stirring. After a reaction for a total time of 2 h, the resultant solid products were washed using ethanol and DW many times and were desiccated at $60^oC$ overnight for. The obtained nanocomposites were then pulverized and annealed at $350^oC$ in $N_2$ atmosphere for 5 h [43]. The same procedures were trailed in the preparation of 0, 50, 70, and 100 % GNPs contents formed nanocomposites.

### 2. 3. Characterization

X-ray diffractometer equipped with Cu $K_\alpha$ ($\lambda$ = 1.5406 Å) radiation (Malvern PANalytical X'pert PRO MPD) was used to obtain the phase of the samples. The morphological investigations of the neat CF nanosheets as well as the composite samples were examined with the help of TEM (Thermo Fisher Tecnai G2 F20). The vibrational modes of the prepared samples were studied using FTIR spectrometer (Bruker). Optical bang gap properties were investigated using UV–visible spectrophotometer, Shimadzu Co., Japan. X-ray photoelectron spectroscopic analysis was carried out using XPS spectrometer (SPECS GmbH, Berlin, Germany) with Al $K_\alpha$ radiation (1486.74 eV).

### 2. 4. Electrochemical analysis

The prepared neat CF nanosheets and the composite samples were investigated for electrochemical characteristics in a symmetric arrangement Swagelok cell with 0.5 M $K_2SO_4$ aqueous electrolyte. The working electrodes were fabricated by the following procedure: a homogeneous paste of PVDF (15 wt. %), active material (75 wt. %), and carbon super P (15 wt. %) in N-Methyl-2-pyrrolidone was prepared. The paste was then spread on aluminum foil and vacuum desiccated at 100$^{o}$C to remove the solvent. Cyclic voltammetry (CV), galvanostatic charge-discharge (GCD) and electrochemical impedance spectroscopy (EIS) were carried out using electrochemical workstation (Biologic VMP3).

### 2. 5. Measurements of photocatalytic activity

The photodegradation of MB using neat CF nanosheets and the composite samples has been measured under irradiation of visible light. For this, 20 mg of prepared materials and 0.7 ml of $H_2O_2$ were added to 100 ml of distilled water solution containing MB (10 mg/L). The reaction was carried out in dark box equipped with Xe light (500 W) source. To attain the adsorption/desorption equilibrium the mixture was stirred for 30 minutes. Afterwards, the test solution was irradiated with the visible light source. About 4 ml aliquots of the test solution were taken at fixed intervals of time, centrifuged and were tested quantitatively to monitor typical absorption peak of MB dye by recording UV-vis absorbance.

## 3. Results and discussions

### 3. 1. Phase and crystallographic investigations

Crystalline structure and phase characteristics of the prepared samples have been analyzed using powder XRD measurements. Comparison of the XRD profiles of CF and $(CF)_{1-x}(GNPs)_x$ samples are given in Fig. 1.

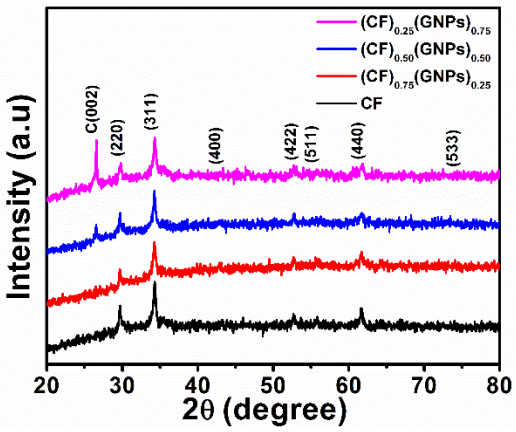


**Fig. 1:** XRD diffractograms of $(CF)_{1-x}(GNPs)_x$ samples.

The Bragg's reflections from $2\theta = 31.17^{o}, 35.44^{o}, 37.02^{o}, 43.4^{o}, 53.7^{o}, 57.3^{o}, 62.7^{o}$ planes of CF are well matched with the (220), (311), (222), (400), (422), (511) and (440) planes (JCPDS No. 78–4321) of the spinel calcium ferrite structure [44]. The peak at $2\theta = 26.32^{o}$, in the XRD patterns of $(CF)_{1-x}(GNPs)_x$ nanocomposites originates from (002) reflection of GNPs, conforming that the composite structure has been synthesized successfully. The absence of peaks corresponding to other extra phases and impurities clearly demonstrates the phase purity of the prepared samples.

### 3. 2. Morphology and microstructure

The morphology morphological examination of as-prepared samples has been carried out by TEM and is presented in Fig. 2.

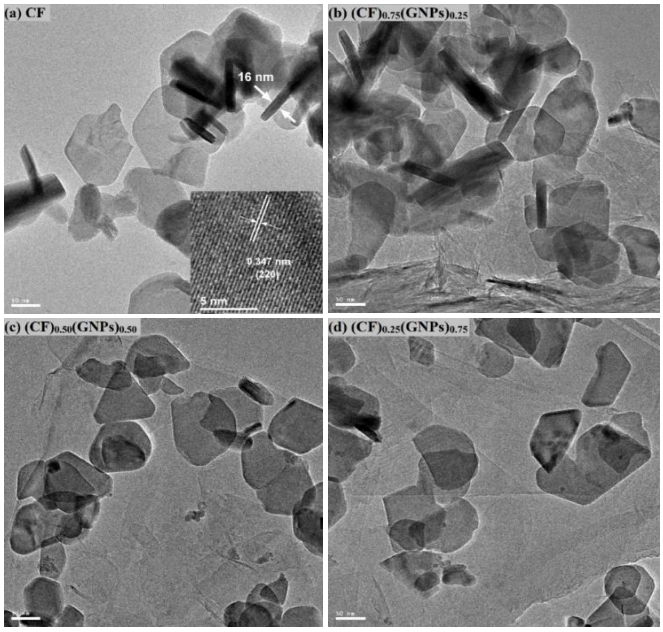


**Fig. 2:** TEM images of $(CF)_{1-x}(GNPs)_x$ materials. HRTEM image of neat CF sample is shown in the inset.

TEM image of neat CF, shown in Fig. 2(a), shows a sheet-like morphology with 16 nm thickness and the sheets appeared to be aggregated together. HRTEM image (inset of Fig. 2) shows the clear lattice fringes, confirming the highly crystalline nature of CF nanosheets. The lattice spacing has been calculated to be 0.347 nm and has been found to be well matched with that of the (220) plane of CF [45]. Fig. 2(b)-(d) represents the TEM images of $(CF)_{1-x}(GNPs)_x$ composites materials. It can be observed that for small GNPs content (25 wt. %) in nanocomposite, CF nanosheets are uniformly attached to the GNPs with minor voids or empty spaces, Fig. 2(b). On the other hand, when the content of GNPs increases, some uncovered surface of GNPs can be observed in Fig. 2 (c)-(d). It means that optimum coverage of GNPs can be achieved by controlling the wt. % ratio of the constituent materials. The unique structure and

morphology of the synthesized $(CF)_{1-x}(GNPs)_x$ composites might present excellent attachment and strong interfacial contact, which may be highly beneficial for the enhancement of photocatalytic and supercapacitive performance of nanocomposite materials.

### 3. 3. Chemical state analysis

The results of XPS study for the prepared $(CF)_{1-x}(GNPs)_x$ nanocomposite are depicted in Fig. 3.

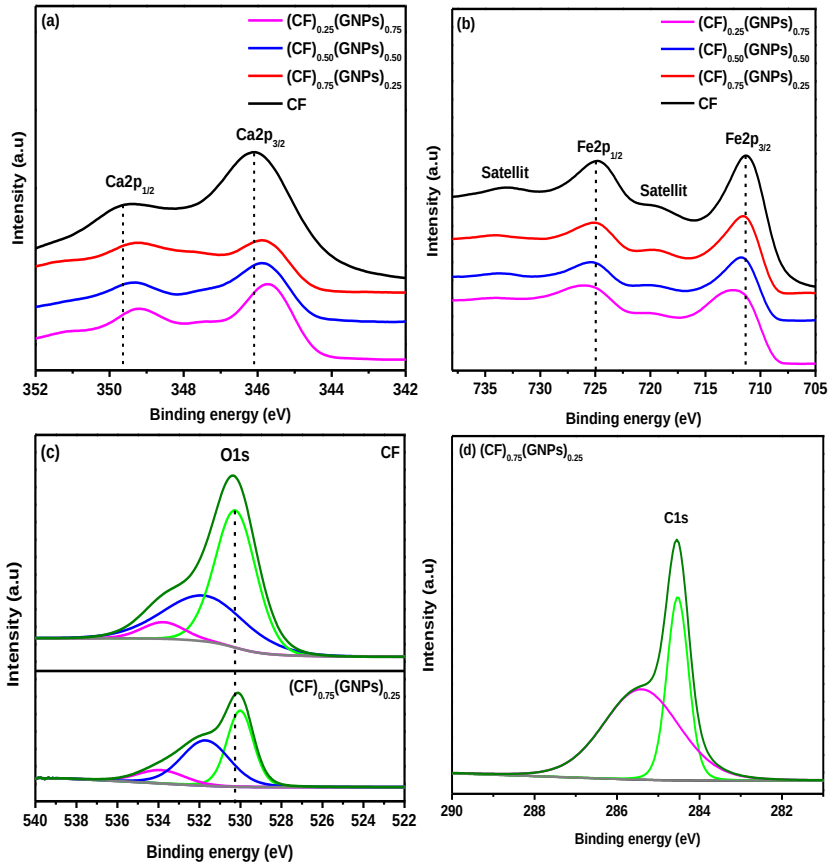


**Fig. 3:** XPS high resolution spectra for $(CF)_{1-x}(GNPs)_x$ materials

XPS technique provides basic information about the crystal defects and valence oxidation state of the materials, both of which play a key role in controlling physiochemical characteristics as well as radiative recombination of charge carriers. The high resolution spectra of Ca 2p shown in Fig. 3(a) consists of two resolved peaks with binding energies located at 346.06 and 349.4 eV, accredited to Ca $2p_{3/2}$ and Ca $2p_{1/2}$ spin states. As illustrated in Fig. 3(b), the peaks at 711.5 eV and 725.3 eV are the Fe $2p_{3/2}$ and Fe $2p_{1/2}$ of CF, respectively [46]. Furthermore, the two satellite peaks are also visible in the Fe 2p spectra of the prepared samples, which, indicate the existence of $Fe^{3+}$ in the prepared samples. Fig. 3(c) shows typical O 1s XPS spectra for $(CF)_{0.75}(GNPs)_{0.25}$ nanocomposite, which indicates that the O1s species exists in

different coordination environment within the sample. The three deconvoluted peaks in the O1s signal are centered at 530.1, 531.9 and 533.7 eV, which can be assigned to metal-oxygen bond (M–O–M), hydroxyl groups (M–O–H) and the surface-adsorbed oxygen, respectively [47]. The M–O–M metal-oxygen peaks are red shifted in $(CF)_{0.75}(GNPs)_{0.25}$ composite relative to that of neat CF sample, which might be due to the formation of Ca−O−C and Fe−O−C covalent bonds [48]. Meanwhile, the two resolved peaks in the C1s spectrum (Fig. 3 (d)) of $(CF)_{0.75}(GNPs)_{0.25}$, located at 284.39 eV and 285 eV arise due to C=C and C−C covalent bonds of GNPs, respectively [49]. It is interesting to note that the Ca 2p and Fe 2p peaks in the synthesized $(CF)_{1-x}(GNPs)_x$ composite materials are slightly shifted towards lower binding energy as compared to that of neat CF sample. These binding energy shifts in the XPS spectra can be explained by the screening effect arising from the strong electronic interaction between different semiconductors. When the heterojunction is formed between two different semiconductors, electron transfer occurs from one semiconductor to the other to bring their Fermi levels to the same value. As a result of the concentration of electrons changes in each semiconductor, which give rise to the electron screening effect. This charge carrier screening effect, in turn, causes a slight shift in the binding energies of constituent atoms [50].

### 3.4 Optical characteristics

The change in optical characteristics of CF nanosheets upon addition of GNPs has been studied using UV−vis spectroscopic technique. The addition of GNPs significantly affects the light absorption ability of CF nanosheets, as shown in Fig. 4(a).

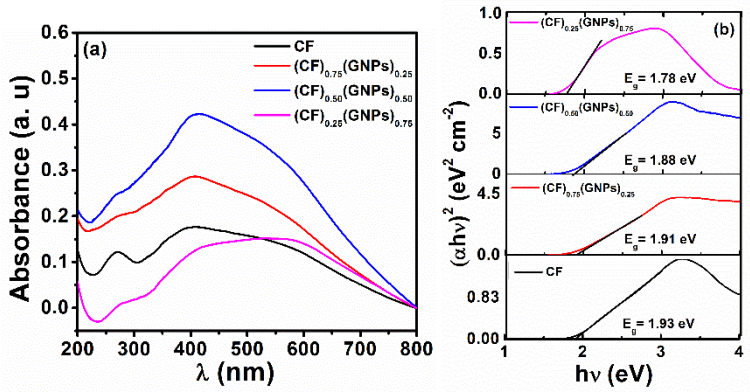


**Fig. 4: (**a) UV-vis spectra, and (b) Tauc's plots of $(CF)_{1-x}(GNPs)_x$ composite materials.

The light absorption of $(CF)_{1-x}(GNPs)_x$ extends into the visible region as compared to CF nanosheets. To analyze the band gap characteristics of the prepared samples, a plot between $(\alpha hv)^2$ versus the energy of light $hv$ has been obtained via the Tauc's relation [51].

$$(\alpha hv)^2 = A(hv - E_g) \tag{1}$$

Here $\alpha, hv, A, and\ E_g$ are absorption coefficients, light energy, constant and optical bandgap energy respectively. The extrapolation of the tangent to $(\alpha hv)^2 = 0$ axis gives band gap energy of a material for direct allowed transitions. As clear from the Tauc's plots, depicted in Fig. 4(b), that the energy band gap decreases consistently with higher loading of GNPs. The band-gaps were estimated to be 1.93, 1.91, 1.88 and 1.78 eV for CF and $(CF)_{1-x}(GNPs)_x$ composites, which shows the decreasing trend in band gap with the increase in wt.% ratio of GNPs. This graphene induced reduction in the band gap can be explained on the basis of strong coupling between CF nanosheets and GNPs. In agreement with XPS results, the chemical bonding of CF nanosheets with GNPs leads to Fe–O–C covalent bond formation in the nanocomposite system. As a consequence, additional energy states are introduced between the valence and conduction band of CF, which in turn cause reduction in band gap energy of $(CF)_{1-x}(GNPs)_x$ nanocomposites [37, 52]. The degree of band gap narrowing increases with increasing the GNPs content in the nanocomposites, because the interaction between CF and GNPs is increased when the mass ratio of GNPs is increased [53].

### 3. 5. FTIR spectroscopy

FTIR spectroscopy is an effective tool to probe the graphene-based nano-systems for the investigation of vibrational modes and surface functional groups. FTIR measurements of the prepared samples are given in Fig. 5.

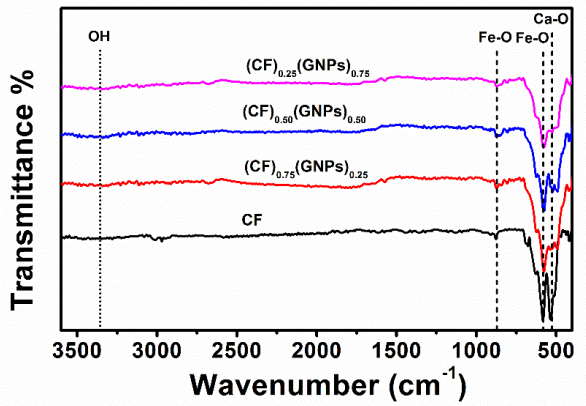


**Fig. 5:** FTIR spectra of $(CF)_{1-x}(GNPs)_x$ nanocomposites.

The transmittance at 536 $cm^{-1}$ is adduced to Ca-O bonds vibrations, whereas the bands at 582 $cm^{-1}$, 875 $cm^{-1}$ indicate the presence of Fe-O stretching modes [29, 33, 54]. Furthermore, the broad absorption bands at 1630 and 3400 $cm^{-1}$, associated with -OH vibrations can be attributed to absorbed water molecules because of sample contact with the environment. The characteristic peaks of Ca-O and Fe-O in the $(CF)_{1-x}(GNPs)_x$ sample are red-shifted as compared to that CF sample. This shift confirms that CF nanosheets are strongly bound to the surface of GNPs [55].

### 3. 6. Photoluminescence spectroscopy

PL measurements have been performed to understand the dependence of interfacial charge transfer and charge carriers recombination in different prepared materials [56, 57].

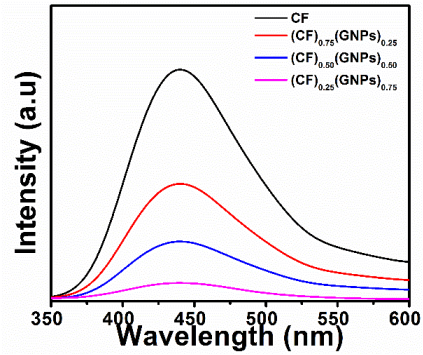


**Fig. 6:** Photoluminescence of $(CF)_{1-x}(GNPs)_x$ nanocomposite samples.

Fig. 6 shows PL spectra of the prepared CF and the $(CF)_{1-x}(GNPs)_x$ nanocomposites. Clearly, the PL intensity consistently decreases as the content of GNPs increases. This decrease in PL intensity indicates that the $e^-/h^+$ pairs recombination is effectively hindered, which can be ascribed to the highly conducting and electron acceptor GNPs [58].

## 4. Electrochemical properties

Electrochemical behavior of prepared electrode materials has been investigated in a two-electrode symmetric device using $(CF)_{1-x}(GNPs)_x$ nanocomposites as active material, glass microfiber separator and 0.5 M $K_2SO_4$ electrolyte.

### 4. 1. CV and GCD analysis

Comparison of the CV profiles obtained for GNPs, CF and $(CF)_{1-x}(GNPs)_x$ nanocomposite samples at 10 $mVs^{-1}$ are given in Fig. 7(a). No Faradic redox peaks have been seen in the obtained CV curves of the prepared electrodes. However, the CV profiles of as-prepared CF, as well as composite electrodes, deviate significantly from the rectangular shape, indicating a Faradic contribution to the overall supercapacitance. It is interesting to note that the CV profile of $(CF)_{0.75}(GNPs)_{0.25}$ electrode has a maximum integrated area, suggesting its superior electrochemical performance. GNPs boosts the conductivity of the nanocomposites, which accelerate the redox reactions and as a consequence electrochemical performance is enhanced [59].

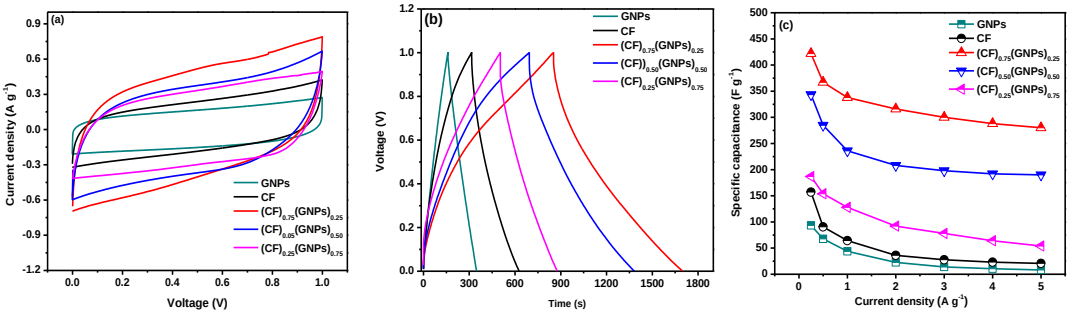


**Fig. 7:** (a) CV profiles at 10 $mVs^{-1}$, (b) GCD profiles at 0.5 $Ag^{-1}$, and (c) specific capacitance curves at different current densities for $(CF)_{1-x}(GNPs)_x$ electrodes.

The supercapacitive performance of the prepared samples has been further examined with the help of GCD technique. Fig. 7 (b) depicts the comparison of GCD curves collected for CF, $(CF)_{1-x}(GNPs)_x$ and GNPs, at 0.25 $Ag^{-1}$. As clear from Fig. 7 (b), the discharge time is longest for the $(CF)_{0.75}(GNPs)_{0.25}$ electrode, which suggests its outstanding electrochemical charge storage capability.

Furthermore, IR drop of $(CF)_{0.75}(GNPs)_{0.25}$ electrode is smaller than that of others, showing its lower overall resistivity and rapid I-V response [60]. The specific capacitance of one electrode (Cs, $Fg^{-1}$) for CF and $(CF)_{1-x}(GNPs)_x$ electrodes has been obtained with the help of the equation [61],

$$C_s = \frac{4I\,\Delta t}{m\Delta V} = 4C_T \tag{2}$$

Here, the discharge time (s), applied potential, current (A), the total mass (g) of active material in both electrodes and specific capacity of the electrochemical cell are represented by $\Delta t$, $\Delta V$, $I$, $m$ and $C_T$ respectively. The specific capacitance for CF, $(CF)_{1-x}(GNPs)_x$ and GNPs, electrodes have been obtained to be 157 $Fg^{-1}$, 422 $Fg^{-1}$, 343.5 $Fg^{-1}$, 187 $Fg^{-1}$ and 93.4 $Fg^{-1}$ respectively. Here, it is important to highlight that significant enhancement has been observed for sample with 25% graphene content. This can be attributed to its unique 2D sheet-on-sheet like morphology and fast charge transport at interfaces, both of which can synergistically lead to the higher specific supercapacitance [62]. However, the specific capacitance decreases at higher graphene ratio (50 wt. % and 75 wt. %). The decreasing trend in specific capacitance at higher loading content of graphene can be adduced to the inferior supercapacitive performance of graphene. As clear from Fig. 7(c), GNPs have smaller supercapacitance, as compared to the other samples, therefore, introducing their higher content (50 wt. % and 75 wt. %) reduces the overall electrochemical capacitance of the nanocomposites. This results has been reported previously [63, 64].

**Table. 1:** Previously reported supercapacitive parameters for symmetric two-electrode cells

| Sample | Electrolyte | Specific capacitance($Fg^{-1}$) | Cycle performance | Reference |
|---|---|---|---|---|
| $NiFe_2O_4$ NR/G | 6 M KOH | 396 at 1 $Ag^{-1}$ | 99% after 10000 cycles | [65] |
| $Fe_2O_3$ NDs@NG | 1 M KOH | 274 at 1 $Ag^{-1}$ | 81.8% after 50000 cycles | [66] |
| $MnFe_2O_4$/rGO | 6 M KOH | 271 at 0.5 $Ag^{-1}$ | 104% after 5000 cycle | [67] |
| $MnFe_2O_4$/graphene | PVA–$H_2SO_4$ | 120 at 0.1 $Ag^{-1}$ | 105% after 5000 cycle | [68] |
| $MnFe_2O_4$/graphene/PANI | 1 M KOH | 307.2 at 0.1 $Ag^{-1}$ | 74% after 2000 cycle | [69] |
| 3D $MnO_2$/graphene | 0.5 M $Na_2SO_4$ | 130 at 2 $mVs^{-1}$ | 82% after 5000 cycle | [70] |
| $NiFe_2O_4$@rGO | $KNO_3$-PVA | 139 at 0.5 $Ag^{-1}$ | 89.8% after 10,000 cycles | [71] |
| 3D $MnO_2$-CNT-G | 1 M $Li_2SO_4$ | 260 1.0 $Ag^{-1}$ | 82% after 3000 cycles | [72] |
| N-$CuMe_2Pc$ | 1 M $H_2SO_4$ | 291.6 at 0.5 $Ag^{-1}$ | 100.1% after 5000 cycles | [73] |
| $V_2O_5$ nanorods/rG | M $LiNO_3$ | 83.5 at 0.5 $Ag^{-1}$ | 34.5% after 1000 cycles | [74] |
| Mn-CPANI | 1 M $H_2SO_4$ | 246 at 1 $Ag^{-1}$ | 97% after 10000 cycles | [75] |
| $CuFe_2O_4$-GN | 3 M KOH | 125.7 at 1 $Ag^{-1}$ | 85% for 1000 cycles | [76] |
| PPy/MG hybrids | 0.5 M $H_2SO_4$ | 205.6 F/g at 0.5 $Ag^{-1}$ | 93% after 30,000 | [77] |
| **$(CF)_{1-x}(GNPs)_x$** | **0.5 M $K_2SO_4$** | **422 at 0.25 $Ag^{-1}$** | **80.7 % after 1500 cycles** | **This work** |

It is interesting to note that the $(CF)_{0.75}(GNPs)_{0.25}$ nanocomposite electrode (Fig. 7(c)) has higher specific capacitance at high current densities as well relative to other prepared samples, indicating its excellent rate capability. The observed enhanced rate performance of the $(CF)_{1-x}(GNPs)_x$ electrodes originates from the effective conducting channels provided by the 2D interfacing of $CaFe_2O_4$ with GNPs.

### 4. 2. Energy-power density, EIS spectra and cyclic stability

The values of energy and power density of the prepared electrode materials have been obtained from the discharging portion of GCD profiles with the help of the following equations [78]**,**

$$Energy\ density = E = \frac{0.5 C_T (\Delta V)^2}{3.6}\ (WhKg^{-1}) \quad (3)$$

$$Power\ density = P = \frac{E}{\Delta t}\ (WKg^{-1}) \quad (4)$$

Here $C_T$, $E$, $\Delta V, P, \Delta t$ are the specific capacitance, average energy density of the cell, the potential window, power density and discharge time, respectively. The energy density calculated for the GNPs, CF and $(CF)_{1-x}(GNPs)_x$ electrodes is 3.26 $WhKg^{-1}$, 5.45 $WhKg^{-1}$, 14.65 $WhKg^{-1}$, 11.92 $WhKg^{-1}$ and 6.49 $WhKg^{-1}$ at 62.5 $WKg^{-1}$ respectively. The Ragone plots are given in Fig. 8 (a)

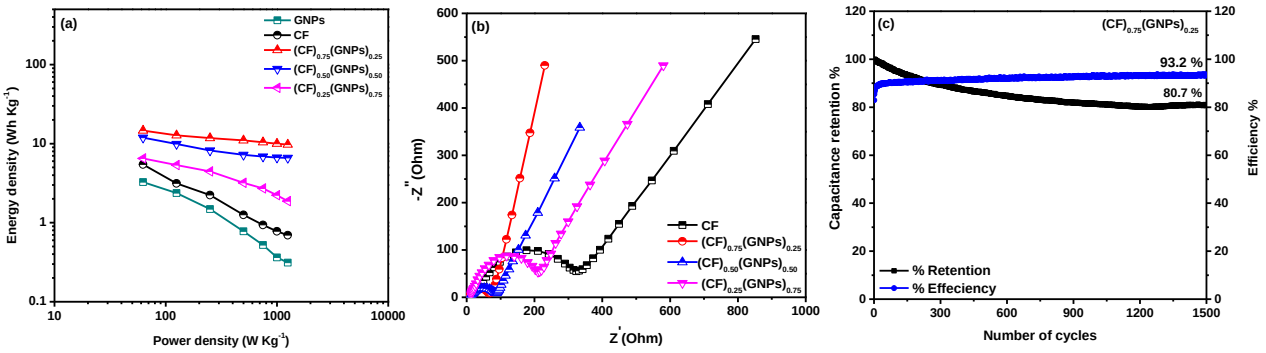


**Fig. 8:** (a) Ragone plots, (b) EIS spectra of $(CF)_{1-x}(GNPs)_x$ electrodes, and (c) cycling stability and Coulombic efficiency of $(CF)_{0.75}(GNPs)_{25}$ electrodes.

It is clear from the Ragone plots that the $(CF)_{1-x}(GNPs)_x$ electrode exhibits outstanding energy density even at higher current densities. This enhanced energy density offered by nanocomposite electrode is attributed to the pseudocapacitive contribution to the overall supercapacitance from 2D CF nanosheets attached to GNPs [79].

The charge storage mechanism of CF and $(CF)_{1-x}(GNPs)_x$ electrodes has been further studied by EIS technique. EIS spectra measured on the complex plane, with frequency range 0.1 Hz-100 kHz and 10 mV bias voltage, have been presented in Fig. 8 (b). The results depict that for the low frequency, the slope of the straight line part corresponds to the ionic resistance of electrolyte. Obviously, $(CF)_{0.75}(GNPs)_{0.25}$ electrode exhibits an almost vertical line as compared to that of other samples, indicating the lowest diffusive resistance. Whereas, in the high-frequency region diameter of semicircle stands for the resistance to charge-transfer at the interface of electrode and electrolyte. It is important to note that the radius of the semicircular part is smallest for $(CF)_{0.75}(GNPs)_{0.25}$ electrode, suggesting that 25 wt.% GNPs content is the optimum value for achieving the lowest interfacial charge-transfer resistance. The 2D nature of the interfaces formed between CF nanosheets and GNPs facilitate the charge transfer, and as a consequence, overall resistivity of the nanocomposite is reduced [80].

The cyclic life of the prepared electrodes has been tested by GCD method for 1500 cycles at 5 $Ag^{-1}$ as shown in Fig. 8 (c). After continuous charging and discharging, the cell retains 80.7% of its maximum capacity. This excellent retention of capacitance undoubtedly demonstrates the better electrochemical reversibility of the $(CF)_{1-x}(GNPs)_x$ electrode material, which could be attributed to the strong mechanical structure and high conductivity of the nanocomposites. GNPs present in the nanocomposite system prevent the aggregation of CF nanosheets during charge/discharge cycle, along with increasing their conductivity. Both of these factors contribute to the improvement of cycling stability of the electrode [81].

## 5. Photocatalytic Activity Test

The photocatalytic decomposition of MB using synthesized CF, $(CF)_{1-x}(GNPs)_x$ and GNPs samples has been carried out under visible light irradiation. The percentage photocatalytic degradation of MB has been calculated using following equation [82].

$$\%\ degradation = \left(1 - \frac{C}{C_o}\right) \times 100 \quad (5)$$

Where $C_o$ and $C$ are the initial and residual concentrations of MB at various intervals of time, respectively. The photodegradation efficiency of CF, $(CF)_{1-x}(GNPs)_x$ nanocomposites and GNPs has been calculated to be 55.6%, 99.4%, 91.2%, 83.1% and 19.8% respectively (for 90 min), as shown in Fig. 9.

Table. 2: Comparison with previous reported literature of photocatalysis

| Photocatalyst | Morphology | Photocatalyst conce. /volume | Amount of photocatalyst | Degradation time/Efficiency | Light source | Reference |
|---|---|---|---|---|---|---|
| $CaFe_2O_4/\alpha\text{-}Fe_2O_3$ | Nanostructures | 10 mg $L^{-1}$/ 100 mL | 30 mg | 180 min/95.7% | 300 W | [83] |
| PAM / $CaFe_2O_4$ | Microspheres | 5 mg $L^{-1}$ /1000 mL | 0.1 g | 180 min/95 % | 500 W | [84] |
| $CaFe_2O_4/g\text{-}C_3N_4$/CNT | Nanoparticles | 10 ppm/100 mL | 0.1 g | 120 min/97% | 300 W | [85] |
| Carbon/$CaFe_2O_4$ | Nanorods | 50 mg $L^{-1}$ / 100 mL | 50 mg | 120 min/93% | 300-W | [86] |
| $CaFe_2O_4/Bi_2O_3$ | Nanoparticles | 10 mg $L^{-1}$ / 100 mL | 0.05 g | 240min/86.9% | 500 W | [87] |
| $CaFe_2O_4/g\text{-}C_3N_4$ | Nanoparticles | 10 mg $L^{-1}$ / 50 mL | 0.1 g | 120 min/94% | 150 W | [88] |
| $ZnFe_2O_4$–rGO | Nanoparticles | 20 mg $L^{-1}$ /100 mL | 20 mg | 150 min /100 % | 500-W | [89] |
| $Fe_3O_4$-GO | Nanoparticles | 20 mg $L^{-1}$ / 500 mL | 0.25 g | 120 min/99% | 500 W | [90] |
| RGO/$Fe_3O_4$ | Nanoparticles | 20 mg $L^{-1}$/100 mL | 25 mg | 120 min/96% | 300 W | [91] |
| $LaFeO_3$/C | Nanoparticles | 15 mg $L^{-1}$ /50 mL | 50 mg | 120 min/85.5% | 300 W | [92] |
| $MnFe_2O_4$-GSC | Nanoparticles | 10 mg $L^{-1}$ /200 mL | 50 mg | 180min/100 % | Sunlight | [93] |
| Zinc ferrite-rGO | Nanostructures | 10 mg $L^{-1}$ / 125 mL | 50 mg | 180 min/ 90% | Sunlight | [94] |
| $(CF)_{1-x}(GNPs)_x$ | 2D Nanosheets | 10 mg $L^{-1}$ /100 mL | 20 mg | 90 min/99.4% | 500 W | This Work |

The $(CF)_{0.75}(GNPs)_{0.25}$ nanocomposite has the highest photocatalytic activity. It is also important to note that the photocatalytic activity decreases by increasing the content of GNPs beyond 25%. To understand the change in photocatalytic activity with GNPs content, the following two factors should be taken into account. 1) According to PL and UV-Vis bandgap results, the photocatalytic activity should increase with increasing content of graphene. 2) The excessive GNPs prevent the light from reaching the active sites on the photocatalyst surface, which reduces the rate of photocatalytic reaction, causing the photodegradation efficiency to reduce [95]. Therefore, photocatalytic activity results from interplay between the two factors.

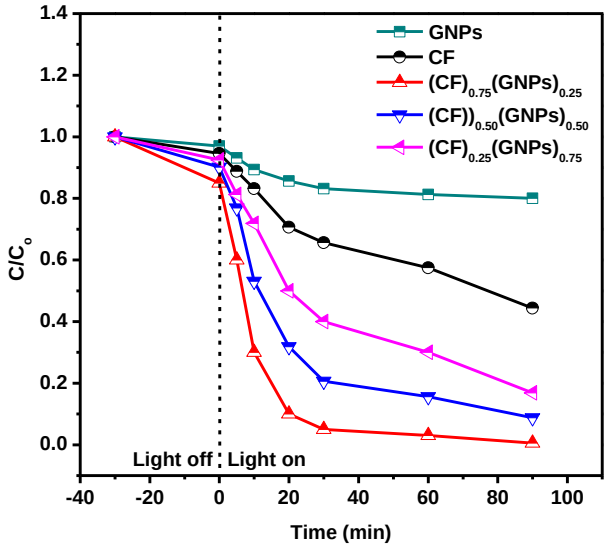


**Fig. 9:** Photodegradation comparison using $(CF)_{1-x}(GNPs)_x$ nanocomposites

At lower graphene ratio, 1st factor is dominant and leads to enhanced photocatalytic activity, while at higher graphene ratio the second factor is dominant resulting in lower photocatalytic activity. Decomposition of MB molecules using $(CF)_{1-x}(GNPs)_x$ nanocomposites has possibly occurred via photo-Fenton and photocatalytic reaction, both. It can be suggested from the observed experimental results that, these two processes synergistically contribute to the enhancement of the photocatalytic activity. The possible mechanism of the photocatalytic reaction can be suggested as shown in Fig. 10.

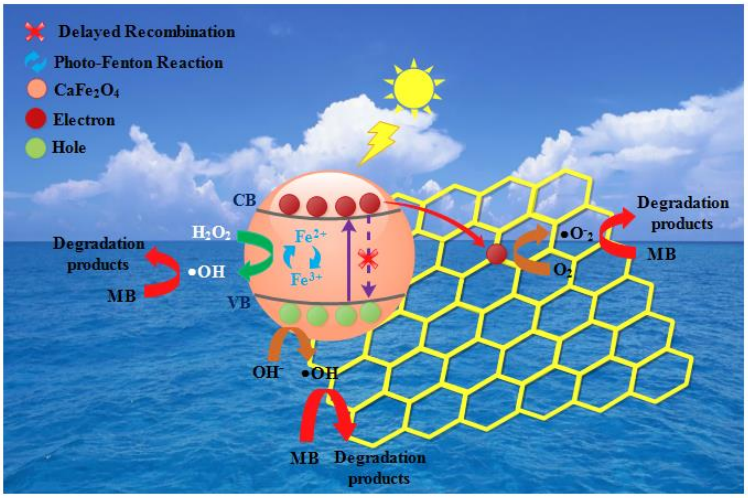


**Fig. 10:** Schematic representation of photodegradation mechanism of MB by $(CF)_{1-x}(GNPs)_x$

In photocatalytic reaction, the electrons are excited to the conduction band (due to light irradiation) producing equal number of holes in the valence band. The electrons are then

transferred to the GNPs present in the composite sample. This effective charge transfer can reduce the rate of $e^-/h^+$ pair recombination, which in turn boosts the efficiency of the photocatalyst. The photoinduced electrons tend to react with absorbed $O_2$ to generate superoxide anion radical ($\bullet O_2^-$), while the holes could also react with surface-bound $H_2O$ and $OH^-$ to produce hydroxy radicals (•OH). The photocatalytic reaction can be expressed as follows [96].

$$CaFe_2O_4 + hv \rightarrow CaFe_2O_4\ (e^- + h^+) \quad (1)$$

$$CaFe_2O_4\ (e^-) + GNPs \rightarrow CaFe_2O_4 + GNPs(e^-) \quad (2)$$

$$GNPs(e^-) + O_2 \rightarrow \bullet\ O_2^- + GNPs \quad (3)$$

$$CaFe_2O_4\ (h^+) + OH^- \rightarrow CaFe_2O_4\ + \bullet\ OH \quad (4)$$

While, in photo-Fenton type reaction, due to the presence of $H_2O_2$, the redox reactions taking place on the surface of the photocatalyst causes mutual conversion of $Fe^{3+}/Fe^{2+}$ ion pairs. $H_2O_2$ decomposes into reactive hydroxyls radicals (•OH) in the presence of light upon interacting with the available active sites ($Fe^{2+}$) over the surface of the photocatalyst. GNPs plays the role in accelerating the photo-Fenton reaction by capturing electrons from $Fe^{2+}$ [97]. The photo-Fenton reaction can be expressed as follows [98]

$$Fe^{3+} + e^- \rightarrow Fe^{2+} \quad (5)$$

$$Fe^{2+} + H_2O_2 \rightarrow Fe^{3+} + \bullet\ OH + H^+ \quad (6)$$

$$Fe^{3+} + hv + OH^- \rightarrow Fe^{2+} + \bullet\ OH \quad (7)$$

These reactive radicals then attack the dye molecules and finally decomposes them into $CO_2$ and $H_2O$. Furthermore, the effective electronic interaction via intimate 2D surface-to-surface contact (as supported by basic characterizations) of the GNPs with CF nanosheets ensures short diffusion lengths for charge transport and fast charge carrier transfer at the interfaces, which enables the nanocomposites to degrade MB with remarkably fast rate [99].

## 5 Conclusions

In this study, $(CF)_{1-x}(GNPs)_x$ nanocomposites having different weight ratios were prepared via cost-effective in situ coprecipitation method and investigated for their performance in electrochemical energy storage and photocatalytic applications. It has been found that the prepared nanocomposites show momentous enhancement in supercapacitive performance in two electrode symmetric cell configuration, however $(CF)_{0.75}(GNPs)_{0.25}$ nanocomposite exhibits the highest specific capacitance. The outstanding supercapacitive performance of the composite electrode at this optimal composition is a consequence of the unique 2D-2D sheet-on-sheet like structure and improved interfacial charge transfer at electrode/electrolyte interface. The prepared $(CF)_{0.75}(GNPs)_{0.25}$ nanocomposite also demonstrates excellent photocatalytic efficiency towards

harmful organic dye under visible light illumination, which is attributed to the reduced charge carrier recombination and effective electronic interaction between the constituents of the nanocomposites. In general, these findings suggest that the physiochemical characteristics can be tuned effectively by tailoring the compositions and the dimensionality, which are crucial for further development of multifunctional graphene-based nanocomposites for electrochemical energy storage and visible light mediated photocatalysis.

**Acknowledgment**

The financial support of this work by the Higher Education Commission of Pakistan (HEC) IRSIP (Grant No: 1-8/HEC/HRD/2017/8412 PIN: IRSIP 39 PSc 15) to M. I. Similarity index is 14% (checked via Turnitin ID: 1338324880).

**References**

1. Kumar, R., et al., *Freestanding 3D Graphene–Nickel Encapsulated Nitrogen-Rich Aligned Bamboo Like Carbon Nanotubes for High-Performance Supercapacitors with Robust Cycle Stability.* Advanced Materials Interfaces, 2015. **2**(15): p. 1500191.
2. Kumar, K.S., et al., *Recent advances in two-dimensional nanomaterials for supercapacitor electrode applications.* ACS Energy Letters, 2018. **3**(2): p. 482-495.
3. Wang, F., et al., *Latest advances in supercapacitors: from new electrode materials to novel device designs.* Chemical Society Reviews, 2017. **46**(22): p. 6816-6854.
4. Gao, X., et al., *Morphology-controllable preparation of NiFe2O4 as high performance electrode material for supercapacitor.* Electrochimica Acta, 2019. **296**: p. 181-189.
5. Fu, M., et al., *Biomass waste derived multi-hierarchical porous carbon combined with CoFe2O4 as advanced electrode materials for supercapacitors.* Journal of Alloys and Compounds, 2019. **782**: p. 952-960.
6. Gao, H., et al., *A general fabrication approach on spinel MCo2O4 (M= Co, Mn, Fe, Mg and Zn) submicron prisms as advanced positive materials for supercapacitor.* 2018. **262**: p. 241-251.
7. Young, C., et al., *One-Step Synthetic Strategy of Hybrid Materials from Bimetallic Metal–Organic Frameworks for Supercapacitor Applications.* 2018. **1**(5): p. 2007-2015.
8. Gao, X., et al., *Morphology-controllable preparation of NiFe2O4 as high performance electrode material for supercapacitor.* 2019. **296**: p. 181-189.
9. Javed, M.S., et al., *Exploring Li-ion hopping behavior in zinc ferrite and promoting performance for flexible solid-state supercapacitor.* 2019. **295**: p. 558-568.
10. Yang, S., et al., *ZnFe2O4 nanoparticles-cotton derived hierarchical porous active carbon fibers for high rate-capability supercapacitor electrodes.* 2018. **134**: p. 15-21.
11. Su, L., et al., *Sprinkling MnFe 2 O 4 quantum dots on nitrogen-doped graphene sheets: the formation mechanism and application for high-performance supercapacitor electrodes.* 2018. **6**(21): p. 9997-10007.
12. Sarac Oztuna, F.E., et al., *Layer-by-Layer Grown Electrodes Composed of Cationic Fe3O4 Nanoparticles and Graphene Oxide Nanosheets for Electrochemical Energy Storage Devices.* The Journal of Physical Chemistry C, 2019.

13. Ahirrao, D.J., K. Mohanapriya, and N. Jha, *V2O5 nanowires-graphene composite as an outstanding electrode material for high electrochemical performance and long-cycle-life supercapacitor.* Materials Research Bulletin, 2018. **108**: p. 73-82.
14. Yang, H., et al., *Graphene-templated synthesis of palladium nanoplates as novel electrocatalyst for direct methanol fuel cell.* Applied Surface Science, 2019. **466**: p. 385-392.
15. Zhu, S., et al., *Hydrothermal synthesis of graphene-encapsulated 2D circular nanoplates of α-Fe2O3 towards enhanced electrochemical performance for supercapacitor.* Journal of Alloys and Compounds, 2019. **775**: p. 63-71.
16. Zhou, Q., Y. Gong, and K. Tao, *Facile one-pot synthesis of 2D vanadium-doped NiCl (OH) nanoplates assembled by 3D nanosheet arrays on Ni foam for supercapacitor application.* Applied Surface Science, 2019.
17. Qiu, D., et al., *In situ synthesis of mesoporous NiO nanoplates embedded in a flexible graphene matrix for supercapacitor electrodes.* Materials Letters, 2018. **232**: p. 163-166.
18. Wang, F., et al., *Advanced Supercapacitors Based on α-Ni (OH) 2 Nanoplates/graphene Composite Electrodes with High Energy and Power Density.* ACS Applied Energy Materials, 2018. **1**(4): p. 1496-1505.
19. Xie, X., et al., *MoS2/Graphene Composite Anodes with Enhanced Performance for Sodium-Ion Batteries: The Role of the Two-Dimensional Heterointerface.* Advanced Functional Materials, 2015. **25**(9): p. 1393-1403.
20. Lingamdinne, L.P., J.R. Koduru, and R.R. Karri, *A comprehensive review of applications of magnetic graphene oxide based nanocomposites for sustainable water purification.* Journal of environmental management, 2019. **231**: p. 622-634.
21. Rajender, G., J. Kumar, and P.J.A.C.B.E. Giri, *Interfacial charge transfer in oxygen deficient TiO2-graphene quantum dot hybrid and its influence on the enhanced visible light photocatalysis.* 2018. **224**: p. 960-972.
22. Liang, J., et al., *Scalable green method to fabricate magnetically separable NiFe2O4-Reduced Graphene Oxide nanocomposites with enhanced photocatalytic performance driven by visible light.* Industrial & Engineering Chemistry Research, 2018. **57**(12): p. 4311-4319.
23. Mukherjee, A., et al., *Visible-Light-Mediated Electrocatalytic Activity in Reduced Graphene Oxide-Supported Bismuth Ferrite.* ACS omega, 2018. **3**(6): p. 5946-5957.
24. Park, C.M., et al., *Potential utility of graphene-based nano spinel ferrites as adsorbent and photocatalyst for removing organic/inorganic contaminants from aqueous solutions: A mini review.* Chemosphere, 2019. **221**: p. 392-402.
25. Charles, A., et al., *Facile synthesis of CaFe2O4 for visible light driven treatment of polluting palm oil mill effluent: Photokinetic and scavenging study.* Science of the Total Environment, 2019. **661**: p. 522-530.
26. Cai, J., S. Li, and G. Qin, *Interface engineering of Co3O4 loaded CaFe2O4/Fe2O3 heterojunction for photoelectrochemical water oxidation.* Applied Surface Science, 2019. **466**: p. 92-98.
27. Cao, J., et al., *Fabrication of p-type CaFe2O4 nanofilms for photoelectrochemical hydrogen generation.* Electrochemistry Communications, 2011. **13**(3): p. 275-278.
28. Sen, S., et al., *Ethanol sensing evaluation of sol–gel barium calcium ferrite.* Ceramics International, 2016. **42**(11): p. 12581-12585.

29. Balasubramanian, P., et al., *A new electrochemical sensor for highly sensitive and selective detection of nitrite in food samples based on sonochemical synthesized Calcium Ferrite (CaFe2O4) clusters modified screen printed carbon electrode.* Journal of colloid and interface science, 2018. **524**: p. 417-426.
30. Sharma, N., et al., *Iron–tin oxides with CaFe2O4 structure as anodes for Li-ion batteries.* Journal of power sources, 2003. **124**(1): p. 204-212.
31. Díez-García, M.I. and R. Gómez, *Investigating water splitting with CaFe2O4 photocathodes by electrochemical impedance spectroscopy.* ACS applied materials & interfaces, 2016. **8**(33): p. 21387-21397.
32. Ida, S., et al., *Preparation of p-type CaFe2O4 photocathodes for producing hydrogen from water.* Journal of the american chemical society, 2010. **132**(49): p. 17343-17345.
33. Vadivel, S., et al., *Facile synthesis of novel CaFe2O4/g-C3N4 nanocomposites for degradation of methylene blue under visible-light irradiation.* Journal of colloid and interface science, 2016. **480**: p. 126-136.
34. An, S., et al., *Enhancement removal of crystal violet dye using magnetic calcium ferrite nanoparticle: study in single-and binary-solute systems.* Chemical Engineering Research and Design, 2015. **94**: p. 726-735.
35. Ong, H.R., et al., *Synthesis and characterization of a CaFe 2 O 4 catalyst for oleic acid esterification.* RSC Advances, 2015. **5**(121): p. 100362-100368.
36. Bagherzadeh, M. and R. Kaveh, *New Magnetically Recyclable Reduced Graphene Oxide rGO/MFe2O4 (M= Ca, Mg)/Ag3PO4 Nanocomposites With Remarkably Enhanced Visible-light Photocatalytic Activity and Stability.* Photochemistry and photobiology, 2018. **94**(6): p. 1210-1224.
37. Han, S., et al., *One-Step Hydrothermal Synthesis of 2D Hexagonal Nanoplates of α-Fe2O3/Graphene Composites with Enhanced Photocatalytic Activity.* Advanced Functional Materials, 2014. **24**(36): p. 5719-5727.
38. Zhang, F., et al., *Exceptional synergistic enhancement of the photocatalytic activity of SnS2 by coupling with polyaniline and N-doped reduced graphene oxide.* Applied Catalysis B: Environmental, 2018. **236**: p. 53-63.
39. Lu, B., et al., *Nanoscale pn heterojunctions of BiOI/nitrogen-doped reduced graphene oxide as a high performance photocatalyst.* carbon, 2018. **132**: p. 191-198.
40. Nagaraju, P., et al., *Rapid synthesis of WO3/graphene nanocomposite via in-situ microwave method with improved electrochemical properties.* Journal of Physics and Chemistry of Solids, 2018. **120**: p. 250-260.
41. Zhu, Z., et al., *One-pot electrodeposition synthesis of Bi2WO6/graphene composites for photocatalytic applications under visible light irradiation.* Ceramics International, 2018. **44**(3): p. 3511-3516.
42. Xu, C., et al., *More effective use of graphene in photocatalysis by conformal attachment of small sheets to TiO2 spheres.* Carbon, 2016. **96**: p. 394-402.
43. Yang, S., et al., *Graphene-based nanosheets with a sandwich structure.* Angewandte Chemie International Edition, 2010. **49**(28): p. 4795-4799.
44. Wang, G., et al., *Synthesis of calcium ferrite nanocrystal clusters for magnetorheological fluid with enhanced sedimentation stability.* Powder Technology, 2017. **322**: p. 47-53.
45. Kim, E.S., et al., *Fabrication of CaFe2O4/TaON heterojunction photoanode for photoelectrochemical water oxidation.* Journal of the american chemical society, 2013. **135**(14): p. 5375-5383.

46. Fu, Y., et al., *Copper ferrite-graphene hybrid: a multifunctional heteroarchitecture for photocatalysis and energy storage.* Industrial & Engineering Chemistry Research, 2012. **51**(36): p. 11700-11709.
47. Yan, W., et al., *One-pot synthesis of monodispersed porous CoFe 2 O 4 nanospheres on graphene as an efficient electrocatalyst for oxygen reduction and evolution reactions.* RSC Advances, 2016. **6**(1): p. 307-313.
48. Mukherjee, A., et al., *Visible-Light-Mediated Electrocatalytic Activity in Reduced Graphene Oxide-Supported Bismuth Ferrite.* 2018. **3**(6): p. 5946-5957.
49. La, D.D., et al., *Fabrication of a GNP/Fe–Mg binary oxide composite for effective removal of arsenic from aqueous solution.* ACS Omega, 2017. **2**(1): p. 218-226.
50. Wang, R., et al., *Preparation of nitrogen-doped TiO2/graphene nanohybrids and application as counter electrode for dye-sensitized solar cells.* ACS Appl. Mater. Interfaces, 2014. **6**(3): p. 2118-2124.
51. Khan, J.A., et al., *Synthesis and characterization of structural, optical, thermal and dielectric properties of polyaniline/CoFe2O4 nanocomposites with special reference to photocatalytic activity.* Spectrochimica Acta Part A: Molecular and Biomolecular Spectroscopy, 2013. **109**: p. 313-321.
52. Soltani, T. and B.-K. Lee, *Sono-synthesis of nanocrystallized BiFeO3/reduced graphene oxide composites for visible photocatalytic degradation improvement of bisphenol A.* Chemical Engineering Journal, 2016. **306**: p. 204-213.
53. Cheng, P., et al., *TiO2–graphene nanocomposites for photocatalytic hydrogen production from splitting water.* international journal of hydrogen energy, 2012. **37**(3): p. 2224-2230.
54. Bilas, R., et al., *Highly biocompatible chitosan with super paramagnetic calcium ferrite (CaFe2O4) nanoparticle for the release of ampicillin.* International journal of biological macromolecules, 2017. **97**: p. 513-525.
55. Le, A.-T., et al., *Enhanced magnetic anisotropy and heating efficiency in multi-functional manganese ferrite/graphene oxide nanostructures.* 2016. **27**(15): p. 155707.
56. Haldar, K.K., et al., *Hybrid colloidal Au-CdSe pentapod heterostructures synthesis and their photocatalytic properties.* ACS applied materials & interfaces, 2012. **4**(11): p. 6266-6272.
57. Shuang-Shuang, Z., et al., *Functionalization of carbon nanotubes/graphene by polyoxometalates and their enhanced photo-electrical catalysis.* Chinese Physics B, 2014. **23**(8): p. 088801.
58. Arshad, A., J. Iqbal, and Q. Mansoor, *NiO-nanoflakes grafted graphene: an excellent photocatalyst and a novel nanomaterial for achieving complete pathogen control.* Nanoscale, 2017. **9**(42): p. 16321-16328.
59. Choi, J., et al., *Fluoride ion-mediated morphology control of fluorine-doped CoFe 2 O 4/graphene sheet composites for hybrid supercapacitors with enhanced performance.* 2018. **279**: p. 241-249.
60. Yan, J., et al., *Fast and reversible surface redox reaction of graphene–MnO2 composites as supercapacitor electrodes.* Carbon, 2010. **48**(13): p. 3825-3833.
61. Shafi, P.M., et al., *α-MnO2/h-MoO3 Hybrid Material for High Performance Supercapacitor Electrode and Photocatalyst.* ACS Sustainable Chemistry & Engineering, 2017. **5**(6): p. 4757-4770.
62. Shen, J., et al., *CoNi2S4-Graphene-2D-MoSe2 as an Advanced Electrode Material for Supercapacitors.* 2016. **6**(13): p. 1600341.

63. Chen, C.-Y., et al., *Tightly connected MnO 2–graphene with tunable energy density and power density for supercapacitor applications.* Journal of Materials Chemistry, 2012. **22**(16): p. 7697-7700.
64. Wang, H., et al., *Asymmetric Supercapacitors Assembled by Dual Spinel Ferrites@ Graphene Nanocomposites as Electrodes.* ACS Applied Energy Materials, 2018. **1**(7): p. 3206-3215.
65. Fu, M., et al., *One-step preparation of one dimensional nickel ferrites/graphene composites for supercapacitor electrode with excellent cycling stability.* Journal of Power Sources, 2018. **396**: p. 41-48.
66. Liu, H., et al., *Easy one-step hydrothermal synthesis of nitrogen-doped reduced graphene oxide/iron oxide hybrid as efficient supercapacitor material.* Journal of Solid State Electrochemistry, 2015. **19**(1): p. 135-144.
67. Tabrizi, A.G., et al., *Facile synthesis of a MnFe 2 O 4/rGO nanocomposite for an ultra-stable symmetric supercapacitor.* New Journal of Chemistry, 2017. **41**(12): p. 4974-4984.
68. Cai, W., et al., *A facile approach to fabricate flexible all-solid-state supercapacitors based on MnFe2O4/graphene hybrids.* Journal of Power Sources, 2014. **255**: p. 170-178.
69. Xiong, P., et al., *Ternary manganese ferrite/graphene/polyaniline nanostructure with enhanced electrochemical capacitance performance.* Journal of Power Sources, 2014. **266**: p. 384-392.
70. He, Y., et al., *Freestanding three-dimensional graphene/MnO2 composite networks as ultralight and flexible supercapacitor electrodes.* ACS nano, 2012. **7**(1): p. 174-182.
71. Zhang, X., et al., *NiFe2O4 nanocubes anchored on reduced graphene oxide cryogel to achieve a 1.8 V flexible solid-state symmetric supercapacitor.* Chemical Engineering Journal, 2019. **360**: p. 171-179.
72. Zhu, G., et al., *Highly conductive three-dimensional MnO 2–carbon nanotube–graphene–Ni hybrid foam as a binder-free supercapacitor electrode.* Nanoscale, 2014. **6**(2): p. 1079-1085.
73. Ramachandran, R., et al., *Synthesis of N-CuMe2Pc nanorods/graphene oxide nanocomposite for symmetric supercapacitor electrode with excellent cyclic stability.* Electrochimica Acta, 2019. **298**: p. 770-777.
74. Liu, H., et al., *Porous V2O5 nanorods/reduced graphene oxide composites for high performance symmetric supercapacitors.* Applied Surface Science, 2019. **478**: p. 383-392.
75. Ghadimi, L.S., et al., *Novel nanocomposite of MnFe2O4 and nitrogen-doped carbon from polyaniline carbonization as electrode material for symmetric ultra-stable supercapacitor.* Electrochimica Acta, 2018. **282**: p. 116-127.
76. Zhang, W., et al., *One-step facile solvothermal synthesis of copper ferrite–graphene composite as a high-performance supercapacitor material.* ACS applied materials & interfaces, 2015. **7**(4): p. 2404-2414.
77. Thu, T.V., et al., *Graphene-MnFe2O4-polypyrrole ternary hybrids with synergistic effect for supercapacitor electrode.* Electrochimica Acta, 2019. **314**: p. 151-160.
78. Zhang, J., et al., *A high-performance asymmetric supercapacitor fabricated with graphene-based electrodes.* Energy & Environmental Science, 2011. **4**(10): p. 4009-4015.

79. Ghosh, D., et al., *High energy density all solid state asymmetric pseudocapacitors based on free standing reduced graphene oxide-Co3O4 composite aerogel electrodes.* 2016. **8**(34): p. 22253-22260.
80. Qu, Q., S. Yang, and X.J.A.m. Feng, *2d sandwich-like sheets of iron oxide grown on graphene as high energy anode material for supercapacitors.* 2011. **23**(46): p. 5574-5580.
81. Xiong, P., H. Huang, and X.J.J.o.P.S. Wang, *Design and synthesis of ternary cobalt ferrite/graphene/polyaniline hierarchical nanocomposites for high-performance supercapacitors.* 2014. **245**: p. 937-946.
82. Wu, Q., et al., *Synthesis and application of rGO/CoFe2O4 composite for catalytic degradation of methylene blue on heterogeneous Fenton-like oxidation.* Journal of the Taiwan Institute of Chemical Engineers, 2016. **67**: p. 484-494.
83. Zhu, Y., et al., *Hydrothermal synthesis of CaFe2O4/α-Fe2O3 composite as photocatalyst and its photocatalytic activity.* Journal of Environmental Chemical Engineering, 2018. **6**(2): p. 3358-3365.
84. Ma, A., L. Zhou, and E.J.M.R.E. Zhang, *Synthesis, magnetic and optical properties and photocatalytic activity of the polyacrylamide decorated CaFe2O4 microspheres for photocatalytic degradation of organic wastewater.* Materials Research Express, 2019. **6**(7): p. 075525.
85. Liu, F., et al., *Synthesis of a well-dispersed CaFe2O4/g-C3N4/CNT composite towards the degradation of toxic water pollutants under visible light.* RSC Advances, 2019. **9**(44): p. 25750-25761.
86. Liu, X., et al., *Visible light-responsive carbon-decorated p-type semiconductor CaFe2O4 nanorod photocatalyst for efficient remediation of organic pollutants.* Chinese Journal of Catalysis, 2017. **38**(10): p. 1770-1779.
87. Luo, D. and Y.J.M.L. Kang, *Synthesis and characterization of novel CaFe2O4/Bi2O3 composite photocatalysts.* Materials Letters, 2018. **225**: p. 17-20.
88. Vadivel, S., et al., *Facile synthesis of novel CaFe2O4/g-C3N4 nanocomposites for degradation of methylene blue under visible-light irradiation.* Journal of colloid and interface science, 2016. **480**: p. 126-136.
89. Yao, Y., et al., *Facile synthesis of magnetic ZnFe 2 O 4–reduced graphene oxide hybrid and its photo-Fenton-like behavior under visible iradiation.* Environmental Science and Pollution Research, 2014. **21**(12): p. 7296-7306.
90. Yu, L., et al., *Degradation of phenol using Fe3O4-GO nanocomposite as a heterogeneous photo-Fenton catalyst.* Separation and Purification Technology, 2016. **171**: p. 80-87.
91. Jiang, X., et al., *New branch on old tree: green-synthesized RGO/Fe3O4 composite as a photo-Fenton catalyst for rapid decomposition of methylene blue.* Ceramics International, 2017. **43**(16): p. 14361-14368.
92. Wang, K., et al., *Immobilizing LaFeO3 nanoparticles on carbon spheres for enhanced heterogeneous photo-Fenton like performance.* Applied Surface Science, 2017. **404**: p. 138-145.
93. Luciano, A.J.R., et al., *Manganese ferrite dispersed over graphene sand composite for methylene blue photocatalytic degradation.* Journal of Environmental Chemical Engineering, 2020: p. 104191.

94. Rani, G.J. and M.J.J.R.o.C.I. Rajan, *Reduced graphene oxide/ZnFe 2 O 4 nanocomposite as an efficient catalyst for the photocatalytic degradation of methylene blue dye.* Research on Chemical Intermediates, 2017. **43**(4): p. 2669-2690.
95. Zhang, Y., et al., *Improving the photocatalytic performance of graphene–TiO 2 nanocomposites via a combined strategy of decreasing defects of graphene and increasing interfacial contact.* Physical Chemistry Chemical Physics, 2012. **14**(25): p. 9167-9175.
96. Fu, Y., et al., *Combination of cobalt ferrite and graphene: high-performance and recyclable visible-light photocatalysis.* Applied Catalysis B: Environmental, 2012. **111**: p. 280-287.
97. Wang, F., et al., *Facile self-assembly synthesis of γ-Fe2O3/graphene oxide for enhanced photo-Fenton reaction.* Environmental Pollution, 2019. **248**: p. 229-237.
98. Fu, Y. and X. Wang, *Magnetically separable ZnFe2O4–graphene catalyst and its high photocatalytic performance under visible light irradiation.* Industrial & Engineering Chemistry Research, 2011. **50**(12): p. 7210-7218.
99. Tu, W., et al., *An In Situ Simultaneous Reduction-Hydrolysis Technique for Fabrication of TiO2-Graphene 2D Sandwich-Like Hybrid Nanosheets: Graphene-Promoted Selectivity of Photocatalytic-Driven Hydrogenation and Coupling of CO2 into Methane and Ethane.* Advanced Functional Materials, 2013. **23**(14): p. 1743-1749.